HHS Public Access

Author manuscript

*Nat Commun*. Author manuscript; available in PMC 2016 January 22.

Published in final edited form as:

*Nat Commun*. ; 6: 5865. doi:10.1038/ncomms6865.

# Evidence for an oxygen evolving iron–oxo–cerium intermediate in iron-catalysed water oxidation

**Zoel Codolà**[1], **Laura Gómez**[2], **Scott T. Kleespies**[3], **Lawrence Que Jr**[3], **Miquel Costas**[1], and **Julio Lloret-Fillol**[1]

[1]Institut de Química Computacional i Catàlisi (IQCC) and Departament de Química, Universitat de Girona, Campus de Montilivi, 17071 Girona, Spain

[2]Department of Chemistry and Center for Metals in Biocatalysis, University of Minnesota, 207 Pleasant St S.E., Minneapolis, Minnesota 55455, USA

[3]Serveis Tècnics de Recerca (STR), Parc Cientific i Tecnològic, Universitat de Girona, 17003 Girona, Spain

## Abstract

The non-haem iron complex $\alpha$-[$Fe^{II}(CF_3SO_3)_2$(mcp)] (mcp = (*N*,*N*′-dimethyl-*N*,*N*′-bis(2-pyridylmethyl)-1,2-*cis*-diaminocyclohexane) reacts with $Ce^{IV}$ to oxidize water to $O_2$, representing an iron-based functional model for the oxygen evolving complex of photosystem II. Here we trap an intermediate, characterized by cryospray ionization high resolution mass spectrometry and resonance Raman spectroscopy, and formulated as [(mcp)$Fe^{IV}$(O) ($\mu$-O)$Ce^{IV}(NO_3)_3]^+$, the first example of a well-characterized inner-sphere complex to be formed in cerium(IV)-mediated water oxidation. The identification of this reactive $Fe^{IV}$–O–$Ce^{IV}$ adduct may open new pathways to validate mechanistic notions of an analogous $Mn^{V}$–O–$Ca^{II}$ unit in the oxygen evolving complex that is responsible for carrying out the key O–O bond forming step.

High-valent iron-oxo species are implicated in important biological and synthetic oxidative transformations[1–3]. Some of these species have also shown a remarkable competence towards water oxidation to form dioxygen, a reaction that involves O-O bond formation[4–7]. The reaction is particularly appealing because it has been recognized as one of the bottleneck challenges for the success of artificial photosynthesis, and the identification of iron compounds as efficient catalysts opens novel directions in the quest for earth-abundant systems that could be used on a large scale[8–11]. In this context, the study of the water oxidation (WO) reaction with chemical oxidants catalysed by well-defined coordination



Correspondence and requests for materials should be addressed to L.Q. (larryque@umn.edu) or to M.C. (miquel.costas@udg.edu) or to J.L.-F. (julio.lloret@udg.edu).

**Author contributions**

J.L.-F. and M.C. devised the initial concept for the work and designed the experiments. Z.C. carried out the WO experiments and trapped the intermediate; L.G. performed the CSI-HRMS studies and analysed the data. S.T.K. obtained the resonance Raman spectra and analysed the data together with L.Q. Z.C., L.Q., M.C. and J.L.-F. wrote the manuscript.

**Additional information**

Supplementary Information accompanies this paper at http://www.nature.com/naturecommunications

**Competing financial interests:** The authors declare no competing financial interests.

complexes can clarify fundamental principles underlying the mechanisms of O-O bond formation and cleavage[12,13], the latter being at the heart of chemical processes by which aerobic organisms respire[14]. Most remarkably, given the strong parallels between the oxidation chemistry of iron and manganese compounds[15], it can be envisioned that fundamental chemical insights extracted from studies of O-O bond formation by iron coordination compounds can shed light on intermediates and mechanisms operating at the Oxygen Evolving Complex (OEC).

We and others have recently shown that non-haem iron complexes containing tetradentate nitrogen-based ligands are competent catalysts for chemically driven WO[4,5,16,17]. In our systematic studies, we determined that the presence of two *cis* labile sites is required for WO activity and that electronic effects modulate the catalytic efficiency, providing basic principles for catalyst design[4,5]. Herein, we present evidence for a catalytically relevant reaction intermediate that precedes the oxidation of the water molecule in the case of $\alpha$-[$Fe^{II}(CF_3SO_3)_2$(mcp)], **1-$\alpha$** (Table 1), which we have identified as a particularly active catalyst. This transient species is characterized by high resolution mass spectrometry (CSI-HRMS) and resonance Raman spectroscopy (rR) as a heterodimetallic oxo-bridged iron-cerium complex formed by the reaction of the oxoiron(IV) complex $\alpha$-[$Fe^{IV}(O)(H_2O)$(mcp)]$^{2+}$ and $Ce^{IV}$. The Fe(O)($\mu$-O)Ce$(OH_2)_n$ core of this intermediate bears a strong structural resemblance to the Mn(O)($\mu$-O)Ca$(OH_2)_2$ unit found in the natural oxygen evolving centre. Most remarkably, the Fe(O)($\mu$-O)Ce$(OH_2)_n$ unit is catalytically competent in water oxidation.

## Results

### Catalytic activity of 1-α and 1-β in water oxidation

[$Fe^{II}(CF_3SO_3)_2$(mcp)] is known to form two topological isomers, **1-$\alpha$** and **1-$\beta$** (Fig. 1)[18–21], which have previously been shown to behave differently as catalysts for C-H and C = C bond oxidations[19,21]. Given this sensitivity, the abilities of both complexes to act as water oxidation catalysts were explored. In a typical reaction, an aqueous solution of **1-$\alpha$** or **1-$\beta$** (0.5 ml, 12.5 μM, final concentration) was added to an aqueous solution of CAN (9.5 ml, 125 mM, pH = 0.8, final concentration and pH). Gases evolved from these reactions were monitored by manometry and quantified by gas chromatography with a thermal conductivity detector (GC-TCD). Under these conditions (Table 1), **1-$\alpha$** was highly active and yielded 160±10 and 380±20 TON of $O_2$, (mol of $O_2$/mol of catalyst) when using 100 and 12.5 μM catalyst concentrations, respectively. In contrast, very small amounts of $O_2$ were detected when the same experiment was carried out with its topological isomer **1-$\beta$** (4 ± 1 and 5 ± 2 TON, respectively). Therefore, despite the fact that the two complexes differed only in their ligand topology, their activities as water oxidation catalysts were found to be drastically different. Besides $O_2$, only small amounts of $CO_2$ were present at the end of the reaction (<1 TON), indicating that no major ligand oxidation occurred during catalytic $O_2$ evolution.

### Spectroscopic characterization

Reactions were then analysed spectroscopically to gain insight into the origin of the marked differences in reactivity (Fig. 2). The reaction of **1-$\alpha$** or **1-$\beta$** with CAN (3 eq.) in $H_2O$ (final

pH = 1) resulted in the formation of ***α***/***β***-$[Fe^{IV}(O)(H_2O)(mcp)]^{2+}$, **2-*α*** or **2-*β***, respectively. Both exhibited near-IR bands characteristic of $Fe^{IV}(O)$ complexes, namely $\lambda_{max}$ = 769 nm ($\varepsilon$ = 270 $M^{-1}$ $cm^{-1}$) for **2-*α*** and $\lambda_{max}$ = 778 nm ($\varepsilon$ = 280 $M^{-1}$ $cm^{-1}$) for **2-*β*** (Fig. 2a,b and Supplementary Fig. 1–2). The use of 2.5 equivalents of $Ce^{IV}$ to fully transform **1-*α*,*β*** to **2-*α*,*β*** may be an indication of the high redox potential necessary to oxidize $Fe^{III}$-$OH_2$ to $Fe^{IV}(O)$ (Fig. 3). Taking into consideration the Nernst equation, the redox potential for the $Fe^{III}$-$OH_2$/$Fe^{IV}(O)$ couple under the low pH reaction conditions is estimated at ~1.4 V versus NHE, which matches that obtained in recent DFT calculations[22].

Formation of **2-*α*** was further confirmed and monitored by CSI-HRMS (Fig. 4a and Supplementary Figs 3–7) and $^1$H-NMR spectroscopy (see Supplementary Figs 8 and 9). The excellent agreement between speciation observed by UV–vis and ESI-MS shows a clean transformation between **1-*α*** and **2-*α*** (Fig. 3). Importantly, the CSI-HRMS spectra of **2-*α*** showed an intense peak at *m/z* = 545.110±0.003 that can be assigned to $\{[Fe^{IV}(O)(mcp)](CF_3SO_3)\}^+$ on the basis of its *m/z* value and isotope distribution pattern. Consistently, the peak moved to 547.117±0.003 when **2-*α*** was generated in $H_2{}^{18}O$, due to the incorporation of $^{18}O$ into the oxo ligand. In addition, a second strong signal at *m/z* = 413.162±0.003 was observed, which shifts to 417.172±0.003 when $H_2{}^{18}O$ was used. Therefore, the peak was assigned to the $[Fe^{IV}(O)(OH)(mcp)]^+$ ion (Supplementary Figs 3–7). These ions may correspond to the respective loss of $H_2O$ and $CF_3SO_3H$ from the parent $\{[Fe^{IV}(O)(OH_2)(mcp)](CF_3SO_3)\}^+$ ion, thus identifying **2-*α*** as $[Fe^{IV}(O)(OH_2)(mcp)]^{2+}$. **2-*α*** could be also prepared by reacting $[Fe^{II}(Cl)_2(mcp)]$ with CAN (3 eq.), providing further evidence for water and not a triflate ion as the sixth ligand. In addition, support for a terminal oxo ligand in **2-*α*** was obtained by rR spectroscopy ($\lambda_{exc}$ = 413.1 nm, −8 °C, in 1:1 $H_2O$:$CH_3CN$), where a resonance enhanced feature was observed at 822 $cm^{-1}$. This feature downshifted by 40 $cm^{-1}$ with the use of $H_2{}^{18}O$ (Fig. 5a), consistent with its assignment to the Fe = O stretch of **2-*α*** [23,24].

Decay of **2-*α*** ($\tau_{1/2}$ = 20 min at 25 °C) did not result in $O_2$ evolution, showing that it cannot be the WO species. In fact, further reaction of **2-*α*** with CAN was necessary to generate the WO species. To investigate the nature of the latter, the reaction of **2-*α*** with an excess of CAN was monitored simultaneously by UV–vis spectroscopy, manometry and CSI-HRMS (Fig. 6, Supplementary Fig. 10). UV–vis spectroscopy and CSI-HRMS were used to monitor the time-dependent evolution of the oxoiron(IV) species, as well as the consumption of $Ce^{IV}$, while $O_2$ evolution within the same time period was determined by manometry and GC-TCD.

Reaction of CAN (75 equiv.) with **2-*α*** resulted in $O_2$ evolution concomitant with $Ce^{IV}$ consumption. After all $Ce^{IV}$ was consumed, $O_2$ evolution stopped and 18.4 TON of $O_2$ (Fig. 2c, Supplementary Fig. 10) were formed. Therefore, 98% of the added CAN was converted productively to $O_2$, (maximum TON = 18.75 based on the initial $Ce^{IV}$ with $n(Ce^{IV})/n(O_2)$ = 4). At this point, 30% of the initial amount of **2-*α*** remained in solution, as judged by its absorbance at $\lambda$ = 769 nm (Supplementary Fig. 10d). The CSI-HRMS spectrum of the solution showed intense peaks at *m/z* = 414.1696 and 739.0270, values that are within experimental error of the exact masses for $[Fe^{III}(mcp)(OH)_2]^+$ and $[(mcp)Fe(O)(OH)Ce(NO_3)_3]^+$ species, respectively; associated isotope distribution patterns are also

consistent with these formulations. The addition of a second aliquot of CAN (75 equiv.) restarted $O_2$ evolution, producing an additional 11 TON of $O_2$ until $Ce^{IV}$ depletion ceased and complete disappearance of the 769 nm band (**2-*α***) was observed (Supplementary Figs 11,12).

The reaction of **2-*α*** with CAN (75 equiv.) elicited the immediate appearance of a broad absorption band in the 500–650 nm range and a hypsochromic shift of the near-IR feature of **2-*α*** (Fig. 2a, Supplementary Fig. 10b). These changes were not observed on addition of triflic acid (TfOH), $Ce^{III}(NO_3)_3$ or $Sc(OTf)_3$ to **2-*α***. Interestingly, the new chromophore gradually diminished in intensity concomitant with $Ce^{IV}$ consumption, and the near-IR band of **2-*α*** re-emerged (albeit with a reduced intensity because of partial decomposition) (Fig. 2a and Supplementary Fig. 10). These observations provide evidence for the accumulation of a novel reaction intermediate, **3-*α***.

The formation of **3-*α*** was further corroborated by a kinetic analysis of the reaction of **2-*α*** with CAN at 25 °C and pH = 1. The initial rates of $Ce^{IV}$ consumption and $O_2$ evolution by **1-*α*** (0.1 mM) showed a saturation behaviour with respect to [$Ce^{IV}$]. In addition, the reaction rate exhibited a linear dependence on **2-*α*** (0.01–1 mM), and in [$Ce^{IV}$] at [$Ce^{IV}$] in the 1.25–12.5 mM range, with a reaction order close to one for both reagents at large Ce/Fe ratios (under pseudo-first order conditions). At [$Ce^{IV}$]>12.5 mM, reaction rates exhibited saturation, becoming independent of [$Ce^{IV}$] (see Supplementary Figs 13–19). This kinetic behaviour indicates a pre-equilibrium binding of $Ce^{IV}$ to **2-*α*** leading to the accumulation of an intermediate, namely **3-*α***, the evolution of which represents the rate determining step of the reaction. We assessed the viability of this notion by analysing the reaction between $Ce^{IV}$ and **2-*α*** to form **3-*α*** in 1:1 v-v $CH_3CN$:$H_2O$ solution at −8 °C, a temperature at which $O_2$ evolution and $Ce^{IV}$ consumption basically ceased. We found that the formation of **3-*α*** is very fast and reversible, with an equilibrium constant $K_{eq}$ of 120(±25) that could be estimated from the titration data (See Supplementary Figs 20–24, Supplementary Tables 1 and 2 and Supplementary Methods). Notably, analogous kinetic observations have been made in WO mediated by [$Fe^{II}(CF_3SO_3)_2$($^{Me,X}$Pytacn)] ($^{Me,X}$Pytacn = 1-(2′-pyridylmethyl)-4,7-dimethyl-1,4,7-triazacyclononane, X = H, Cl, $CO_2Et$, $NO_2$), suggesting the possibility of a common pathway for WO by these two non-haem iron WO catalysts[5].

Like **1-*α***, the topological isomer **1-*β*** reacted with CAN (3 eq.) to form the $S = 1$ *β*-[$Fe^{IV}$(O)($OH_2$)(mcp)]$^{2+}$ (**2-*β***, $\lambda_{max}$ = 753 nm, $\varepsilon$ = 280 $M^{-1}$ $cm^{-1}$) as judged by UV–vis, CSI-HRMS and $^1$H-NMR (See Supplementary Fig. 1, right, Supplementary Figs 3, 8 and 9). However, in contrast to **2-*α***, the reaction of **2-*β*** with CAN (75 equiv.) did not result in a significant decrease in the concentration of CAN nor was $O_2$ evolution observed (Fig. 2d). Moreover, the formation of a putative **3-*β*** was not observed. Given the structural similarity between **2-*α*** and **2-*β***, the failure of the latter to elicit water oxidation, together with the kinetic similarities between **2-*α*** and the catalytically active [$Fe^{II}(CF_3SO_3)_2$($^{Me,X}$Pytacn)] complexes[5], strongly suggests that the formation of **3-*α*** is required for WO to proceed.

### Characterization of intermediate 3-*α*

CSI-HRMS experiments shed some light on the nature of **3-*α*** that was formed in the reaction of **2-*α*** with $Ce^{IV}$ under catalytic conditions ([Fe] = 1 mM; [CAN] = 75 mM, Fig. 4, Supplementary Figs 25 and 26). The addition of CAN caused the disappearance of the peak at *m/z* = 545.110 corresponding to **2-*α*** (Fig. 4b) and the appearance of a new peak at *m/z* 738.0235 and designated as $\mathbf{M_3}$, which was not observed when **1-*β*** was treated with excess of CAN (Supplementary Fig. 27).

The composition of $\mathbf{M_3}$ was deduced with the aid of isotopic labelling. When $H_2{}^{18}O$ was used as a solvent, $\mathbf{M_3}$ upshifted by four units (Fig. 4e). As the oxygen atoms of the nitrates do not undergo fast exchange with $H_2{}^{18}O$ (see Supplementary Fig. 28), this upshift suggests that $\mathbf{M_3}$ must contain two oxygen atoms capable of facile exchange with water. In contrast, experiments with $D_2O$ showed that $\mathbf{M_3}$ does not have exchangeable protons (Fig. 4d). Furthermore, the isotopic distribution pattern of $\mathbf{M_3}$ could only be correctly simulated by taking into account the natural abundance isotopes of one Fe and one Ce atom. Specifically, the $^{54}Fe$ isotope (5.8% relative to $^{56}Fe$) is responsible for the $\mathbf{M_3}-2$ peak, while the $^{142}Ce$ isotope (11.1% relative to $^{140}Ce$) contributes significantly to the $\mathbf{M_3}$ + 2 peak (Supplementary Fig. 29). Taken together, these results allow $\mathbf{M_3}$ to be formulated as $\{[Fe^{IV}(O)_2(mcp)Ce^{IV}(NO_3)_3]\}^+$ (calc. *m/z* 738.0245, found *m/z* 738.0235) (For further details see Supplementary Methods). This formulation requires the replacement of one hydrogen atom from the $[Fe^{IV}(O)(OH)(mcp)]^+$ ion (*m/z* 413.1616) by the $[Ce^{IV}(NO_3)_3]^+$ moiety to give rise to $\mathbf{M_3}$.

Collision induced dissociation (CID) MS/MS experiments at different collision energies (CE) were performed for $\mathbf{M_3}$ (*m/z* = 738.0). At relative low energies (12 eV), the CID fragmentation of $\mathbf{M_3}$ + H led to the loss of a neutral $HNO_3$ (*m/z* = 676.0). Only at CE higher than 24 eV did the parent peak at 738.0 disappear, but the *m/z* 676.0 ion (corresponding to neutral loss of $HNO_3$ from $\mathbf{M_3}$ + H) persisted at even higher collision energies (up to 39 eV). These results indicate the robustness of the $\{Fe^{IV}\text{-}O\text{-}Ce^{IV}\}$ moiety in the gas phase (Supplementary Fig. 30).

Decisively, Fig. 6 shows that the decay of $\mathbf{M_3}$ (monitored by CSI-HRMS) parallels the decrease in the intensity of the 615 nm chromophore attributed to **3-*α***. Such a correlation indicates that $\mathbf{M_3}$ in fact corresponds to **3-*α***. Taken together, the spectroscopic results and the kinetic model that arises from analysing $Ce^{IV}$ consumption and $O_2$ evolution establishes **3-*α*** as the last detectable and catalytically competent intermediate in water oxidation.

The molecular structure derived from the MS analysis indicates that **3-*α*** corresponds to $\mathbf{M_3}$, but the ion may also contain additional water ligands bound at Ce(IV) in the solution state that would be readily lost in the gas phase. This proposal is supported by the fact that Ce(IV) forms kinetically labile and dynamic complexes with a coordination number of 8 to 9. Furthermore, recent Ce(IV) speciation and quantum dynamic studies have shown a fast ligand exchange at the coordination sphere of Ce(IV)[25–27].

More detailed insight into the nature of the iron-cerium adduct was provided by rR spectroscopy of liquid samples maintained at −8 °C in a 1:1 $H_2O$:MeCN solvent mixture.

UV–vis and mass spectrometry characterization of **2-*a*** and **3-*a*** in this solvent mixture indicates that their identities are the same as in pure water (Supplementary Table 3). This temperature was employed to stabilize **3-*a*** sufficiently so as to be characterized by rR. Furthermore, under these conditions, $O_2$ production also correlates with decay of **3-*a*** (Supplementary Fig. 31). As shown in Fig. 5, the rR spectrum ($\lambda_{ex}$ = 413.1 nm, Fig. 5a) of **2-*a*** prepared with 3 equiv. of $Ce^{IV}$ exhibits a feature at 822 $cm^{-1}$ that downshifts to 782 $cm^{-1}$ on replacing $H_2{}^{16}O$ by $H_2{}^{18}O$, consistent with its assignment to the $\nu_{Fe=O}$ of **2-*a***. Near-UV excitation was required to observe this feature as **2-*a*** has insignificant absorbance in the visible region, as found for other non-haem oxoiron(IV) complexes[23,24].

Interestingly, the rR spectra of **3-*a*** obtained with the same excitation wavelength ($\lambda_{ex}$ = 413.1 nm, Fig. 5b) also show the 822 $cm^{-1}$ vibration and its downshift to 782 $cm^{-1}$ upon $H_2{}^{18}O$ substitution. This feature may arise from either **2-*a*** or **3-*a*** or both species. To clarify, we compared the intensities of the 822 $cm^{-1}$ peaks for the **2-*a*** (3-CAN) and **3-*a*** (9-CAN) samples relative to the adjacent 762-$cm^{-1}$ nitrate feature as an internal standard, after taking into account that the 9-CAN sample has three times the amount of nitrate as the 3-CAN sample. Indeed, the two samples are found to have 822 $cm^{-1}$ peaks of comparable intensity. Given an association constant of 120(±25) $M^{-1}$ (in agreement with a $K_{eq}$ of 90(±10) $M^{-1}$ under catalytic conditions, at 25 °C in $H_2O$, obtained by the kinetic analysis of $O_2$ evolution, Supplementary Fig. 19) for the interaction of **2-*a*** with CAN from UV–vis titration experiments, it is expected that **3-*a*** would account for ~80% of the iron in the Raman samples. Therefore, the 822 $cm^{-1}$ $\nu_{Fe=O}$ vibration observed in the 9-CAN samples must arise mainly from **3-*a***.

Notably, a second feature of similar intensity appears at 677 $cm^{-1}$ with 413.1 nm excitation in the sample of **3-*a*** (Fig. 5b). This lower-frequency feature persists when **3-*a*** is probed with 514.5 nm excitation, a wavelength at which only **3-*a*** has an absorption feature, but the 822 $cm^{-1}$ vibration is not observed, consistent with the absorption features associated with the $Fe^{IV}$ = O unit[26,27]. With either excitation wavelength, the 677 $cm^{-1}$ peak downshifts to 643 $cm^{-1}$ on replacing $H_2{}^{16}O$ by $H_2{}^{18}O$, but is not affected when the experiment was carried out in $D_2O$ (Supplementary Figs 32–33). The 34 $cm^{-1}$ downshift is consistent with a diatomic Fe–O vibration, but the lower frequency indicates a weaker Fe–O bond that is also resonance-enhanced with 514.5 nm excitation on Ce-adduct formation. Fe–O modes in this frequency range have previously been reported for complexes with $Fe^{III}(\mu\text{-}O)_2Fe^{IV}$ (666 $cm^{-1}$)[28,29] and $Fe^{IV}{}_2(\mu\text{-}O)_2$ (674 $cm^{-1}$)[30] cores, respectively, suggesting the possibility of forming an analogous $Fe^{IV}(\mu\text{-}O)_2Ce^{IV}$ core, which would be consistent with the elemental composition of **3-*a*** determined by CSI-HRMS. To test whether this feature could arise from an $Fe^{IV}(\mu\text{-}O)_2Ce^{IV}$ diamond core, rR experiments on **3-*a*** were performed in a 1:1 $H_2{}^{16}O$:$H_2{}^{18}O$ solvent mixture. Under these conditions, the rR spectrum exclusively shows peaks at 677 and 643 $cm^{-1}$, with no peak found at an intermediate frequency that could be associated with a mixed-labelled diamond core (See Supplementary Fig. 32)[31]. The $H_2{}^{16}O$:$H_2{}^{18}O$ experiment thus excludes formation of an $Fe^{IV}(\mu\text{-}O)_2Ce^{IV}$ core. We have also considered the possibility that the 677 $cm^{-1}$ vibration may correspond to the Fe–OH–Ce mode of an O = $Fe^{IV}$–OH–$Ce^{IV}$ core, as earlier postulated[5]. However, two points argue against this possibility: (a) the lack of a $D_2O$ effect on the 677 $cm^{-1}$ vibration[32] and (b)

more importantly, the fact that Fe–OH–Fe vibrations are typically found in the range of 400–500 $cm^{-1}$ (refs [32,33]) much lower than observed for **3-*α***. Consideration of the above points together with its mass spectral formulation leads us to favour an O = $Fe^{IV}$–O–$Ce^{IV}$ core for **3-*α***. An analogous heterodimetallic $Fe^{IV}$–O–$Sc^{III}$ unit has been characterized crystallographically by Fukuzumi and Nam[34], but unfortunately there is no Raman data reported for comparison.

## Discussion

Identification of **3-*α*** with an O = $Fe^{IV}$–O–$Ce^{IV}$ core as the key reaction intermediate in WO reactions introduces unconsidered mechanistic scenarios for the oxidation of water by $Ce^{IV}$ (Fig. 7). Most obviously, $Ce^{IV}$ appears not to behave simply as an outer-sphere oxidant, but instead forms an inner-sphere $Fe^{IV}$(μ-O)$Ce^{IV}$ intermediate that is crucial for the reaction to proceed. Therefore, $Ce^{IV}$-driven Fe-based WO activity not only requires the presence of two *cis*-labile sites but also a structure of the iron complex that allows formation of the $Fe^{IV}$(μ-O)$Ce^{IV}$ intermediate. In this regard, the contrasting reactivities of **1-*α*** and **1-*β*** may arise from differences in their steric or electronic properties. A possible rationale comes from the differences in the nature of the donor *trans* to the *cis*-labile sites of the *α* and *α* isomers. While the *α* isomer has two tertiary amines *trans* to the labile positions, the *β* isomer has one tertiary amine and one pyridine. From our earlier survey of non-haem iron WO catalysts, the more active complexes are similar to **1-*α*** with two tertiary amines *trans* to the two labile sites, whereas **1-*β***, like the [$Fe^{II}(CF_3SO_3)_2$(tpa)] complex (tpa = tris(2-pyridylmethyl)amine), has lower WO activity[4]. In contrast, close inspection of the crystallographic data for **1-*β*** (ref. 19) shows that the N-Me groups point towards the *cis*-labile sites in such a way that might inhibit for formation of oxo-bridged dinuclear species (Supplementary Fig. 34). Although examination of simple ***β***-[(mcp)$Fe^{IV}$(*μ*-O)$Ce^{IV}(NO_3)_3]^+$ models seems to discard this possibility, a survey of the literature reveals that **1-*α*** can form a number of oxo-bridged diferric complexes that have been crystallographically characterized, but dimeric species derived from **1-*β*** are at present not known[35].

How intermediate **3-*α*** evolves further to produce $O_2$ remains unclear[36]. In Fig. 7 are postulated two possible mechanism an oxo/oxyl radical coupling mechanism to form the O–O bond (Path **a**, Fig. 7)[12] and the alternative hypothesis entailing electron transfer from $Fe^{IV}$ to $Ce^{IV}$ to generate a highly electrophilic {$Fe^{V}$(O)(μ-O)$Ce^{III}$} oxidant (Fig. 7, path **b**). Water binding to the $Ce^{III}$ would position it well for electrophilic attack by the $Fe^{V}$ = O moiety to form the O–O bond. This pathway is analogous to that proposed for **1**-catalysed C-H and C = C oxidations with $Ce^{IV}$ as an oxidant[37]. Also supporting the notion of a highly electrophilic oxidant are the observed effects of substituents on the pyridine of the supporting ligand of a related catalyst on WOC efficacy, where more electron withdrawing substituents on the pyridine ligand enhance both TON and TOF for water oxidation[5]. Nevertheless, at this point it is not possible to discard the other scenarios unequivocally.

The [$Fe^{IV}$(O)(μ-O)$Ce^{IV}$] intermediate we have characterized resembles the corresponding $Mn^{V}$(O)(*μ*-O)$Ca^{II}(OH_2)$ unit proposed in some mechanistic models for the OEC (Fig. 8),[38–40] making **3-*α*** an iron-based functional OEC model. In fact, the resemblance becomes stronger with electron transfer from $Fe^{IV}$ to $Ce^{IV}$ to generate an [$Fe^{V}$(O)(μ-O)$Ce^{III}$] oxidant.

The strong similarities between iron and manganese chemistry in biologically relevant oxidation reactions suggest that this analogy should not be unexpected. Also relevant is the fact that $Ce^{III}$ can replace $Ca^{II}$ in biomolecules or act as an antagonist in pharmacology[41–43]. For example, it has been found that lanthanides, Ce in particular, are essential for the growth of *Methylacidiphilum fumariolicum* SoIV[41], while $Ca^{II}$ can be replaced by $Ce^{III}$ in the pyrroloquinoline quinone (PQQ)-dependent methanol dehydrogenanse (MDH) enzymes to elicit superior catalytic properties[41,42].

The mechanisms for O–O bond formation currently being considered for the OEC can be grouped in two main paths: (a) a nucleophilic attack of a water molecule to a $Mn^{V}{\equiv}O$ (or a $Mn^{IV}$-oxyl, $Mn^{IV} = O\ \cdot$) unit, and (b) an oxo/oxyl radical coupling mechanism[40,44,45]. Remarkable mechanistic insight into the O–O bond formation reaction has been obtained from studies of Mn (refs [38,39,46]) and Co (refs [47–50]) tetrametallic cubane model complexes. Up to now these cubane OEC models generally support the oxo/oxyl radical coupling mechanism to form the O–O bond. However, there are no catalytically active WO models that include in their structure a Lewis acid to mimic the role of $Ca^{II}$ in PSII (refs [38,39,46,51,52]), despite the fact that a Lewis acid ($Ca^{II}$, but also $Sr^{II}$)[53,54] has been proven to be absolutely required for the operation of the OEC. Given their obvious interest, the absence of heterodimetallic complexes that are active in water oxidation may reflect the extraordinary difficulty in accessing well-defined models where both a first row transition metal centre and a Lewis acid work together in water solution[50]. The success of our effort to trap and characterize **3-*α*** as having an [$O = Fe^{IV}$-O-$Ce^{IV}$] core that resembles the fundamental $Mn^{V}(O)(\mu\text{-}O)Ca(OH_2)_2$ structural motif of the OEC unit is therefore remarkable from an inorganic synthesis perspective. More importantly, the identification of an [$O = Fe^{IV}$-O-$Ce^{IV}$] core that is active in water oxidation provides a model compound to study the formation of the O–O bond in detail.

In conclusion, this work provides experimental evidence and characterization of an $Fe^{IV}$–O–$Ce^{IV}$ species as the last detectable intermediate in Fe-catalysed WO reactions. Although Ru–O–Ce intermediates have been proposed in water oxidation reactions by different research groups[55–58], to the best of our knowledge this is the first direct experimental characterization of a heterodimetallic core in a synthetic WO catalyst. Furthermore, the $Fe^{IV}$–O–$Ce^{IV}$ active species we have described in this work can be construed as the closest structural and functional model for the essential heteodimetallic $Mn^{V}$–O–$Ca^{II}$ centre involved in the water oxidation event in PSII.

## Methods

### Materials

Reagents were purchased from commercial sources and used as received, without any further purification. Cerium(IV) ammonium nitrate (CAN) (≥99.99%) and trifluoromethanesulfonic acid (ReagentPlus grade ≥99%) were purchased from Sigma-Aldrich. Solvents were purchased from SDS and Scharlab, purified and dried by passing through an activated alumina purification system (MBraun SPS-800) and stored in an anaerobic glovebox under $N_2$. Complexes **1-*α*** and **1-*β*** were prepared as previously described. Water (18.2 MΩ cm) was purified with a Milli-Q Millipore Gradient AIS system.

### Physical methods

UV–vis-NIR spectra were recorded on an Agilent 8453 diode array spectrophotometer (190–1,100 nm range) in 1-cm quartz cells. A cryostat from Unisoku Scientific Instruments was used for temperature control. The amount of gas generated was measured with a differential pressure transducer sensor (Honeywell-ASCX15DN, ±15 psi). Each reaction had its own reference reaction, which was connected to the other port of the sensor. Further details of the equipment are available elsewhere[4,5].

### High resolution mass spectra

High resolution mass spectra were recorded on a Bruker MicrOTOF-Q II instrument with ESI or Cryospray ionization sources at Serveis Tècnics of the University of Girona. Samples were introduced into the mass spectrometer ion source by direct infusion using a syringe pump and were externally calibrated using sodium formate. The instrument was operated in the positive ion mode.

### Resonance raman spectroscopy

Resonance Raman (rR) spectra were collected via excitation with $Kr^+$ and $Ar^+$ lasers (Spectra-Physics BeamLok 2060-RM) and an Acton AM-506M3 monochromator equipped with a Princeton Instruments ACTON PyLON LN/CCD-1340 × 400 detector. Low-temperature spectra in $H_2O$:$CH_3CN$ solution mixtures were obtained at 265 K using a 90° backscattering geometry. Raman frequencies were calibrated to indene before data collection. Rayleigh scattering was attenuated using a holographic notch filter (Kaiser Optical Systems) for each excitation wavelength. The monochromator slit width was set for a band pass of 4 $cm^{-1}$ for all spectra. All spectra were collected using a laser excitation power of 100 mW. The plotted spectra are averages of 96 scans with collection times of 20 s. All spectra were intensity-corrected to the 922 $cm^{-1}$ peak of the $CH_3CN$ solvent.

### Kinetic studies

The required amount of iron complex was dissolved with 2.7 ml of Milli-Q water in a quartz UV–vis cell at 25 °C. Then, the $Fe^{IV}(O)(H_2O)$ intermediate was generated by the addition of 3 equiv. of CAN dissolved in 50 μl of diluted HOTf (3:10, HOTf:$H_2O$). Once fully formed, Milli-Q water (0.25 ml) was added to the solution. A second addition of CAN in 0.3 ml of HOTf:$H_2O$ (at pH~0) was added. This second addition leads to the desired final concentration of $Ce^{IV}$ (ranged from 1.25 to 18.75 mM) and iron complex (0.1 mM) for the kinetic studies at pH = 1. Cerium(IV) consumption was monitored at $\lambda$ = 420 nm. Oxygen evolution was monitored in parallel by a pressure transducer. The initial rate method was applied to obtain rate constants in the kinetic studies to avoid interference of the consumption of the catalysts during the catalytic reactions. All the kinetic data were treated following the same procedure. Only data obtained within the first 10 s of reaction was used, which corresponds to the decay of 20% of the starting Ce absorbance. From these data, the self-decay of a $Ce^{IV}$ blank experiment (same concentration, pH = 1) was subtracted. For the transformation of the absorbance to concentration, blank samples for every $Ce^{IV}$ concentration were linearized and the equation was used as a calibration curve.

## Supplementary Material

Refer to Web version on PubMed Central for supplementary material.

## Acknowledgments

We thank Dr. Xavi Ribas and Dr. Anna Company for reading this work and for helpful comments. We also thank the European Research Foundation for project FP7-PEOPLE-2010-ERG-268445 (J.L.-F), MICINN for project CTQ2009-08464 (M.C.) and for a Ramon y Cajal contract (J.L.-F.), Generalitat de Catalunya for an ICREA Academia Award and the European Research Foundation for Project ERC-2009-StG-239910 (M.C.). The work carried out at the University of Minnesota was supported by US National Institutes of Health grant GM38767 to L.Q. We appreciate financial support from INNPLANTA project INP-2011-0059-PCT-420000-ACT1 to Dr. X. Ribas.

## References

1. Gunay A, Theopold KH. C—H bond activations by metal oxo compounds. Chem Rev. 2010; 110:1060–1081. [PubMed: 20143877]
2. Shaik S, Hirao H, Kumar D. Reactivity of high-valent iron–oxo species in enzymes and synthetic reagents: a tale of many states. Acc Chem Res. 2007; 40:532–542. [PubMed: 17488054]
3. Liu X, Wang F. Transition metal complexes that catalyze oxygen formation from water: 1979–2010. Coord Chem Rev. 2012; 256:1115–1136.
4. Lloret-Fillol J, et al. Efficient water oxidation catalysts based on readily available iron coordination complexes. Nat Chem. 2011; 3:807–813. [PubMed: 21941254]
5. Codolà Z, et al. Electronic effects on single-site iron catalysts for water oxidation. Chem Eur J. 2013; 19:8042–8047. [PubMed: 23712731]
6. Ellis WC, McDaniel ND, Bernhard S, Collins TJ. Fast water oxidation using iron. J Am Chem Soc. 2010; 132:10990–10991. [PubMed: 20698652]
7. Hoffert WA, Mock MT, Appel AM, Yang JY. Incorporation of hydrogen-bonding functionalities into the second coordination sphere of iron-based water-oxidation catalysts. Eur J Inorg Chem. 2013:3846–3857.
8. Wiechen M, Berends HM, Kurz P. Water oxidation catalysed by manganese compounds: from complexes to ‘biomimetic rocks’. Dalton Trans. 2012; 41:21–31. [PubMed: 22068958]
9. Cao R, Lai W, Du P. Catalytic water oxidation at single metal sites. Energy Environ Sci. 2012; 5:8134–8157.
10. Yagi M, Kaneko M. Molecular catalysts for water oxidation. Chem Rev. 2000; 101:21–36. [PubMed: 11712192]
11. Nocera DG. The Artificial Leaf. Acc Chem Res. 2012; 45:767–776. [PubMed: 22475039]
12. Kundu S, et al. O–O bond formation mediated by a hexanuclear iron complex supported on a stannoxane core. Chem Eur J. 2012; 18:2787–2791. [PubMed: 22262528]
13. Kodera M, et al. Reversible O–O bond scission of peroxodiiron(III) to high-spin oxodiiron(IV) in dioxygen activation of a diiron center with a bis-tpa dinucleating ligand as a soluble methane monooxygenase model. J Am Chem Soc. 2012; 134:13236–13239. [PubMed: 22839735]
14. Ferguson-Miller S, Babcock GT. Heme/copper terminal oxidases. Chem Rev. 1996; 96:2889–2908. [PubMed: 11848844]
15. Company, A.; Lloret-Fillol, J.; Costas, M. Comprehensive Inorganic Chemistry II. 2nd. Reedijk, J.; Poeppelmeier, K., editors. Elsevier; 2013. p. 487-564.
16. Hong D, et al. Water oxidation catalysis with nonheme iron complexes under acidic and basic conditions: homogeneous or heterogeneous? Inorg Chem. 2013; 52:9522–9531. [PubMed: 23895380]
17. Chen G, Chen L, Ng SM, Man WL, Lau TC. Chemical and visible-light-driven water oxidation by iron complexes at pH 7–9: evidence for dual-active intermediates in iron-catalyzed water oxidation. Angew Chem Int Ed. 2013; 52:1789–1791.

18. Knof U, von Zelewsky A. Predetermined chirality at metal centers. Angew Chem Int Ed. 1999; 38:302–322.
19. Costas M, Que L Jr. Ligand topology tuning of iron-catalyzed hydrocarbon oxidations. Angew Chem Int Ed. 2002; 41:2179–2181.
20. Costas M, Tipton AK, Chen K, Jo DH, Que L Jr. Modeling rieske dioxygenases: the first example of iron-catalyzed asymmetric cis-dihydroxylation of olefins. J Am Chem Soc. 2001; 123:6722–6723. [PubMed: 11439071]
21. Hong S, et al. Ligand topology effect on the reactivity of a mononuclear nonheme iron(IV)-oxo complex in oxygenation reactions. J Am Chem Soc. 2011; 133:11876–11879. [PubMed: 21736350]
22. Acuña-Parés F, Codolà Z, Costas M, Luis M, Lloret-Fillol J. Unraveling the mechanism of water oxidation catalyzed by nonheme iron complexes. Chem Eur J. 2014; 20:5696–5707. [PubMed: 24668499]
23. Jackson TA, et al. Axial ligand effects on the geometric and electronic structures of nonheme oxoiron(IV) complexes. J Am Chem Soc. 2008; 130:12394–12407. [PubMed: 18712873]
24. Wang D, et al. Nonheme oxoiron(IV) complexes of pentadentate N5 ligands: spectroscopy, electrochemistry, and oxidative reactivity. Chem Sci. 2013; 4:282–291. [PubMed: 23227304]
25. Ikeda-Ohno A, Hennig C, Weiss S, Yaita T, Bernhard G. Hydrolysis of tetravalent cerium for a simple route to nanocrystalline cerium dioxide: an in situ spectroscopic study of nanocrystal evolution. Chem Eur J. 2013; 19:7348–7360. [PubMed: 23630017]
26. Lutz OMD, Hofer TS, Randolf BR, Weiss AKH, Rode BM. A QMCF-MD investigation of the structure and dynamics of Ce4+ in aqueous solution. Inorg Chem. 2012; 51:6746–6752. [PubMed: 22651096]
27. Piro NA, Robinson JR, Walsh PJ, Schelter EJ. The electrochemical behavior of cerium(III/IV) complexes: Thermodynamics, kinetics and applications in synthesis. Coord Chem Rev. 2014; 260:21–36.
28. Wilkinson EC, et al. Raman signature of the $Fe_2O_2$ “Diamond” core. J Am Chem Soc. 1998; 120:955–962.
29. Skulan AJ, Hanson MA, Hsu H-f, Que L Jr, Solomon EI. Spectroscopic Study of $[Fe_2O_2(5\text{-}Et_3\text{-}TPA)_2]^{3+}$: nature of the $Fe_2O_2$ diamond core and its possible relevance to high-valent binuclear non-heme enzyme intermediates. J Am Chem Soc. 2003; 125:7344–7356. [PubMed: 12797809]
30. Xue G, Fiedler AT, Martinho M, Münck E, Que L Jr. Insights into the P-to-Q conversion in the catalytic cycle of methane monooxygenase from a synthetic model system. Proc Natl Acad Sci USA. 2008; 105:20615–20620.
31. Que L Jr, Tolman WB. Bis(μ-oxo)dimetal “Diamond” cores in copper and iron complexes relevant to biocatalysis. Angew Chem Int Ed. 2002; 41:1114–1137.
32. Zheng H, Zang Y, Dong Y, Young VG, Que L Jr. Complexes with $Fe^{III}_2(\mu\text{-}O)(\mu\text{-}OH)$, $Fe^{III}_2(\mu\text{-}O)_2$, and $[Fe^{III}_3(\mu_2\text{-}O)_3]$ cores: structures, spectroscopy, and core interconversions. J Am Chem Soc. 1999; 121:2226–2235.
33. Cranswick MA, et al. Protonation of a peroxodiiron(III) complex and conversion to a diiron(III/IV) intermediate: implications for proton-assisted O–O bond cleavage in nonheme diiron enzymes. Inorg Chem. 2012; 51:10417–10426. [PubMed: 22971084]
34. Fukuzumi S, et al. Crystal structure of a metal ion-bound oxoiron(IV) complex and implications for biological electron transfer. Nat Chem. 2010; 2:756–759. [PubMed: 20729896]
35. Stubna A, et al. A structural and Mössbauer study of complexes with $Fe_2(\mu\text{-}O(H))$ cores: stepwise oxidation from $Fe^{II}(\mu\text{-}OH)_2Fe^{II}$ through $Fe^{II}(\mu\text{-}OH)_2Fe^{III}$ to $Fe^{III}(\mu\text{-}O)(\mu\text{-}OH)Fe^{III}$. Inorg Chem. 2004; 43:3067–3079. [PubMed: 15132612]
36. Halfen JA, et al. Reversible cleavage and formation of the dioxygen O-O bond within a dicopper complex. Science. 1996; 271:1397–1400. [PubMed: 8596910]
37. Garcia-Bosch I, et al. Iron-catalyzed C-H hydroxylation and olefin cis-dihydroxylation using a single-electron oxidant and water as the oxygen-atom source. Chem Eur J. 2012; 18:13269–13273. [PubMed: 22976825]
38. Kanady JS, Tsui EY, Day MW, Agapie T. A synthetic model of the Mn3Ca subsite of the oxygen-evolving complex in photosystem II. Science. 2011; 333:733–736. [PubMed: 21817047]

39. Tsui EY, Tran R, Yano J, Agapie T. Redox-inactive metals modulate the reduction potential in heterometallic manganese-oxido clusters. Nat Chem. 2013; 5:293–299. [PubMed: 23511417]
40. Cox N, Pantazis DA, Neese F, Lubitz W. Biological water oxidation. Acc Chem Res. 2013; 46:1588–1596. [PubMed: 23506074]
41. Pol A, et al. Rare earth metals are essential for methanotrophic life in volcanic mudpots. Environ Microbiol. 2014; 16:255–264. [PubMed: 24034209]
42. Jakupec, MA.; Unfried, P.; Keppler, BK. Reviews of Physiology, Biochemistry and Pharmacology. Vol. 153. Springer; 2005. Pharmacological properties of cerium compounds; p. 101-111.
43. Nakagawa T, et al. A catalytic role of XoxF1 as La3+-dependent methanol dehydrogenase in Methylobacterium extorquens AM1. PLoS ONE. 2012; 7:e50480. [PubMed: 23209751]
44. Rapatskiy L, et al. Detection of the water-binding sites of the oxygen-evolving complex of photosystem II using W-band $^{17}O$ electron–electron double resonance-detected nmr spectroscopy. J Am Chem Soc. 2012; 134:16619–16634. [PubMed: 22937979]
45. Siegbahn PEM. Water oxidation mechanism in photosystem II, including oxidations, proton release pathways, O—O bond formation and $O_2$ release. Biochim Biophys Acta. 2013; 1827:1003–1019. [PubMed: 23103385]
46. Dismukes GC, et al. Development of bioinspired $Mn_4O_4$ – cubane water oxidation catalysts: lessons from photosynthesis. Acc Chem Res. 2009; 42:1935–1943. [PubMed: 19908827]
47. Symes MD, Surendranath Y, Lutterman DA, Nocera DG. Bidirectional and unidirectional PCET in a molecular model of a cobalt-based oxygen-evolving catalyst. J Am Chem Soc. 2011; 133:5174–5177. [PubMed: 21413703]
48. McCool NS, Robinson DM, Sheats JE, Dismukes GC. A $Co_4O_4$ “Cubane” water oxidation catalyst inspired by photosynthesis. J Am Chem Soc. 2011; 133:11446–11449. [PubMed: 21739983]
49. Berardi S, et al. Photocatalytic water oxidation: tuning light-induced electron transfer by molecular $Co_4O_4$ cores. J Am Chem Soc. 2012; 134:11104–11107. [PubMed: 22716164]
50. Evangelisti F, Güttinger R, Moré R, Luber S, Patzke GR. Closer to photosystem II: A $Co_4O_4$ cubane catalyst with flexible ligand architecture. J Am Chem Soc. 2013; 135:18734–18737. [PubMed: 24279370]
51. Leeladee P, et al. Valence tautomerism in a high-valent manganese–oxo porphyrinoid complex induced by a lewis acid. J Am Chem Soc. 2012; 134:10397–10400. [PubMed: 22667991]
52. Lacy DC, Park YJ, Ziller JW, Yano J, Borovik AS. Assembly and properties of heterobimetallic $Co^{II/III}$-$Ca^{II}$ complexes with aquo and hydroxo ligands. J Am Chem Soc. 2012; 134:17526–17535. [PubMed: 22998407]
53. Ono, T-a; Inoue, Y. Discrete extraction of the Ca atom functional for $O_2$ evolution in higher plant photosystem II by a simple low pH treatment. FEBS Lett. 1988; 227:147–152.
54. Boussac A, Rutherford AW. Nature of the inhibition of the oxygen-evolving enzyme of photosystem II induced by sodium chloride washing and reversed by the addition of calcium(2 +) or strontium(2 +). Biochemistry. 1988; 27:3476–3483.
55. Murakami M, et al. Catalytic mechanism of water oxidation with single-site ruthenium–heteropolytungstate complexes. J Am Chem Soc. 2011; 133:11605–11613. [PubMed: 21702460]
56. Yoshida M, Masaoka S, Abe J, Sakai K. Catalysis of mononuclear aquaruthenium complexes in oxygen evolution from water: a new radical coupling path using hydroxocerium(IV) species. Chem Asian J. 2010; 5:2369–2378. [PubMed: 20857479]
57. Kimoto A, Yamauchi K, Yoshida M, Masaoka S, Sakai K. Kinetics and DFT studies on water oxidation by $Ce^{4+}$ catalyzed by $[Ru(terpy)(bpy)(OH_2)]^{2+}$ Chem Commun. 2012; 48:239–241.
58. Wasylenko Derek J, et al. Berlinguette electronic modification of the $[Ru^{II}(tpy)(bpy)(OH_2)]^{2+}$ scaffold: effects on catalytic water oxidation. J Am Chem Soc. 2010; 45:16094–16106. [PubMed: 20977265]

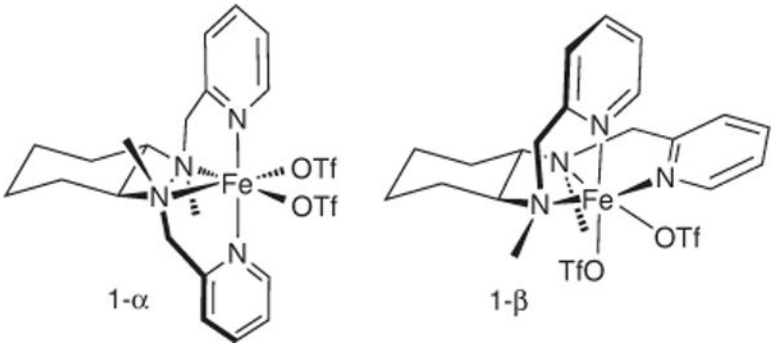


**Figure 1. Iron water oxidation catalysts**

Schematic structure of the iron complexes used in this study.

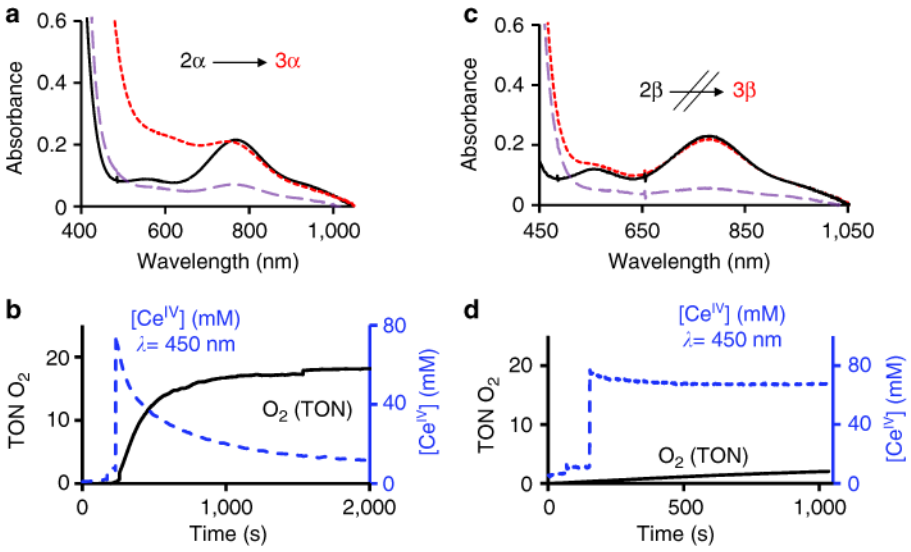


**Figure 2. Real-time manometry/UV–vis monitoring of oxygen evolution and cerium(IV) consumption**

UV–vis spectra of (**a**) **2-*α*** and (**c**) **2-*β*** (solid black line) formed by the respective reactions of **1-*α*** and **1-*β*** (1 mM) in Milli-Q $H_2O$ at 25 °C with 3 equiv. of CAN, on addition of 75 equiv. of CAN (dotted red line) and after CAN consumption (dashed purple line). Time courses for the reaction of (**b**) **1-*α*** and (**d**) **1-*β*** with 75 equiv. CAN monitoring, [$Ce^{IV}$] (right axis, dotted blue line), and $O_2$ evolution (left axis, solid black line). Kinetic traces for [$Ce^{IV}$] were monitored at 450 nm. Δ[$O_2$] (TON) was monitored by a pressure transducer and quantified by GC-TCD.

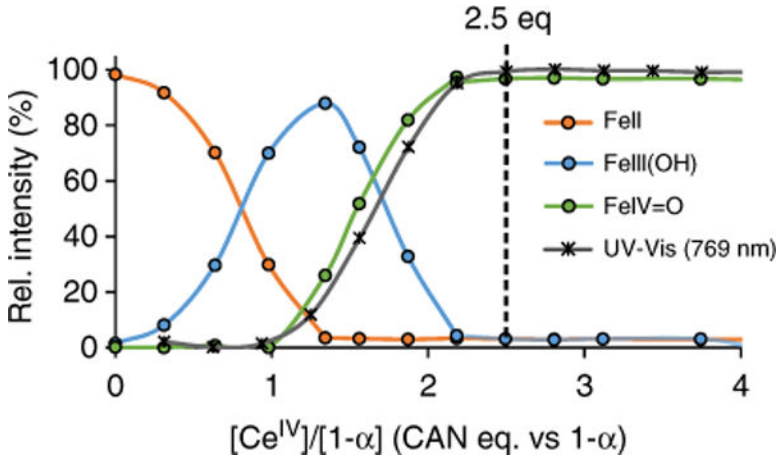


**Figure 3. $Fe^{II}(OH_2)$ to $Fe^{IV}(O)$ titration with $Ce^{IV}$ monitored by UV–vis and HRMS**

Distribution of **$Fe^{II}$**, **$Fe^{III}$** and **$Fe^{IV}$** species according to relative ion peak intensities obtained by HRMS in the titration of **2-*a*** with $Ce^{IV}$. The UV–vis titration (formation of $Fe^{IV}$ = O monitored at 769 nm) was also superimposed in the plot (black crosses).

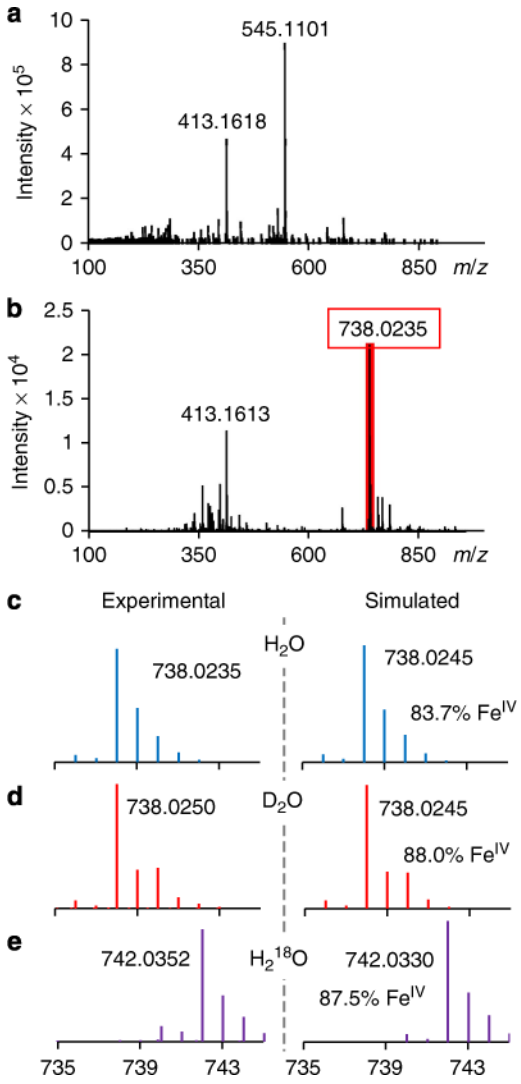


**Figure 4. Characterization of 3-*a* by high resolution mass spectrometry**

(**a**) CSI-HRMS spectrum of **2-*a***, recorded immediately after the oxidation of **1-*a*** (1 mM) by CAN (3 mM). (**b**) CSI-HRMS spectrum obtained during the WO reaction, on the addition of 75 equiv. of CAN to **2-*a***. (**c**–**e**) CSI-HRMS features associated with **3-*a*** obtained in $H_2O$, $D_2O$ and $H_2{}^{18}O$ as solvent. Spectra were recorded by setting the nebulizer and dry gas temperature of the cryospray instrument to 25 °C.

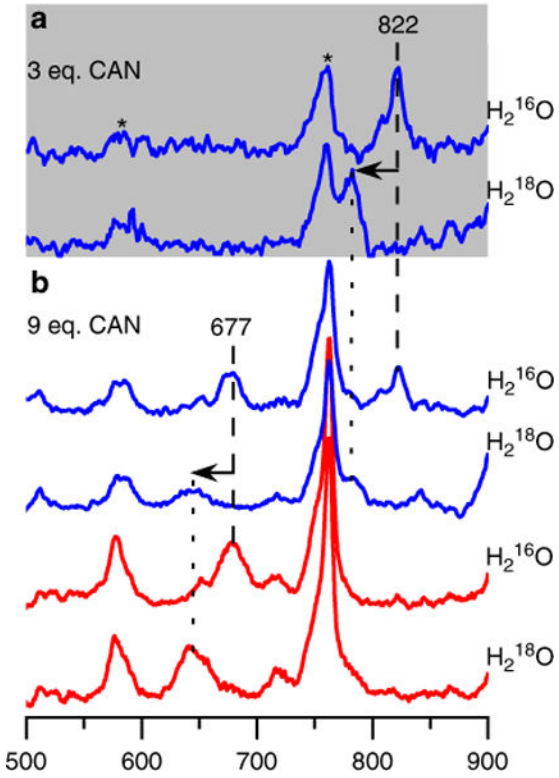


**Figure 5. Characterization of reaction intermediates by Resonance Raman**

(**a**) Highlighted in grey, rR spectra of **2-*a*** ($\lambda_{ex}$ 413.1 nm, 100 mW) prepared on addition of 3 equiv. CAN to a solution of **1-*a*** (5 mM) in 1:1 $H_2O$:MeCN. (**b**) rR spectra of **3-*a*** prepared on addition of 9 equiv. CAN to a solution of **1-*a*** in 1:1 $H_2O$:MeCN. Blue: $\lambda_{ex}$ = 413.1 nm, 100 mW, [Fe] = 5 mM. Red: $\lambda_{ex}$ = 514.5 nm, 100 mW, [Fe] = 8 mM. All spectra were collected from liquid solutions maintained at −8 °C. Asterisks denote features arising from CAN. The intensity of the MeCN solvent peak at 922 $cm^{-1}$ was used to normalize the intensities of the peaks among the various spectra.

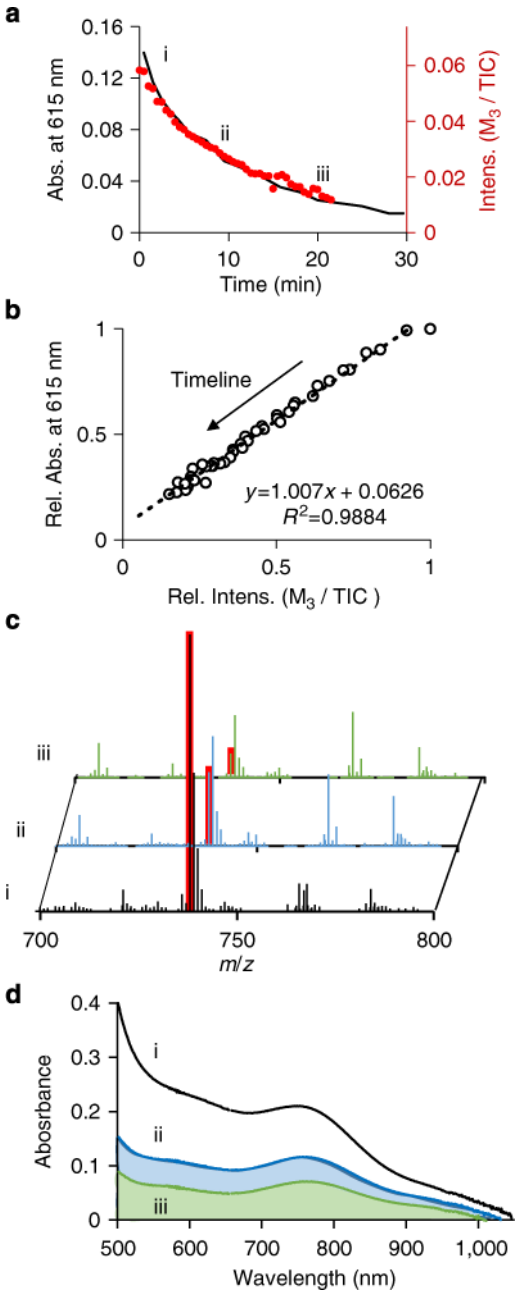


**Figure 6. Decay of 3-*α* monitored by UV–vis and HRMS**

(**a**) Time course for the decay of the 615 nm chromophore (line, left axis) and the $\mathbf{M_3}$ MS peak intensity (dots, right axis) during the reaction of **1-*α*** (1 mM) with CAN (75 mM) at 25 °C. (**b**) Correlation between the relative absorbance ($Abs^t/Abs^0$) at 615 nm and ion count $[(\mathbf{M_3}/TIC)^t/(\mathbf{M_3}/TIC)^0$ of $\mathbf{M_3}$.(*t* = time of measurement;. TIC = total ion count). (**c**,**d**) Mass and visible spectra observed at 10 s (i), 10 min (ii) and 20 min (iii) after the addition of CAN (75 equiv.) to **2-*α*** (1 mM in Milli-Q water, 25 °C).

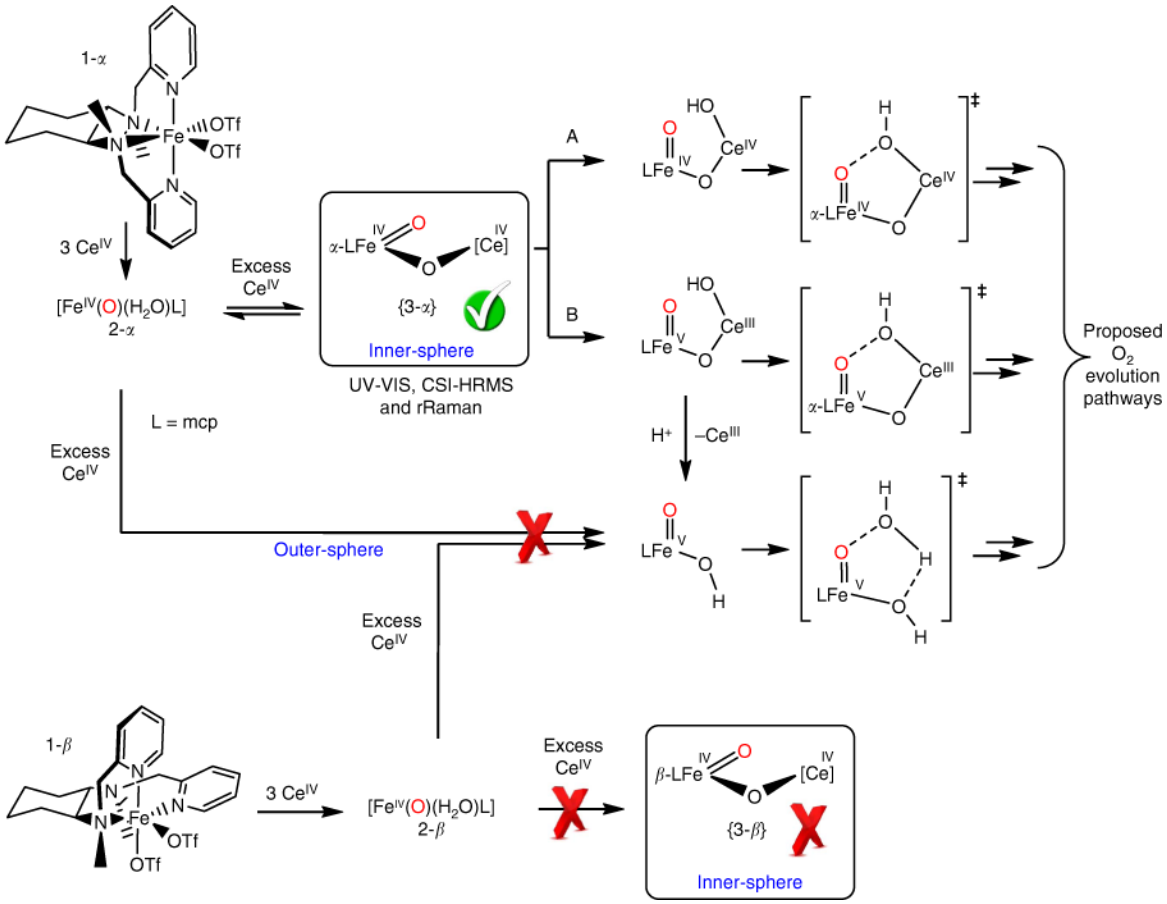


**Figure 7. Reactivity differences between topological isomers α-β**

The mechanism is based on the formation of **3-*α*** as key intermediate for the $O_2$ evolution. Mechanism **a** describes the oxo/oxyl radical coupling between $Fe^{IV}(O)$ and $Ce^{IV}(OH)$. Path (**b**) describes the formation of $Fe^{V}(O)$ and the subsequent nucleophilic attack of a water molecule.

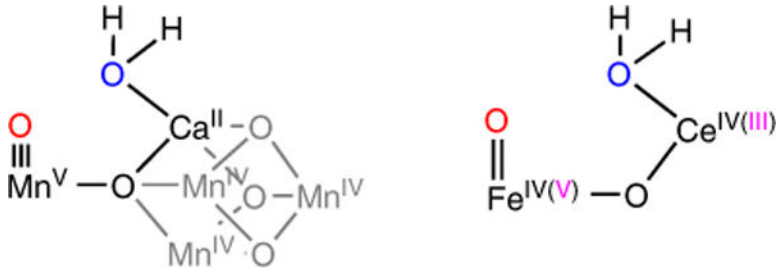


**Figure 8. Structure of the active species and analogy to the proposed intermediate of the OEC**

Analogy between a proposed oxygen evolving complex intermediate and the iron-cerium adduct (**3-*α***), both active species for the water oxidation, containing a metal in a high oxidation state and a Lewis acid, which may orientate the water molecule for the nucleophilic attack.

**Table 1**

Water oxidation catalytic activities for 1-*α* and 1-*β*.

| Catalyst | [cat] (μM) | TON $O_2$* | TOF ($h^{-1}$)† | TON $O_2$‡ | TON $CO_2$‡ |
|---|---|---|---|---|---|
| **1-*α*** | 100 | 110±10 | 580±30 | 160±10 | 0.3±0.2 |
| | 12.5 | 360±20 | 1,020±90 | 380±20 | 0.4±0.2 |
| **1-*β*** | 100 | 4±1 | 9±1 | 4±1 | 0.2±0.1 |
| | 12.5 | 8±2 | 25±11 | 5±2 | 1.1±0.1 |

Reactions performed in Milli-Q water at 25 °C. The catalyst (0.5 ml) was injected through a septum into the reaction vessel containing CAN aqueous solution, (9.5 ml, 131 mM; final concentration 125 mM). The initial pH value was 0.8.

*TON (turnover number) = (n ($O_2$) produced / n(catalyst)) obtained by manometry.

†TOF (TON · $h^{-1}$) measured 5 min after the addition of the catalyst.

‡Values measured by GC-TCD after 3 h of reaction.